JGR Space Physics

Key Points:
- An ephemeral red arc appeared at 68° MLat ($L \approx 7.1$) for 7 min coinciding with a pseudo breakup at 71–72° MLat
- Swarm A/C measurements identified the red arc location at the trough minimum with a localized enhancement of the electron temperature
- The ephemeral red arc may represent a moment of SAR arc birth

An Ephemeral Red Arc Appeared at 68° MLat at a Pseudo Breakup During Geomagnetically Quiet Conditions

S. Oyama[1,2,3] [iD], A. Shinbori[1] [iD], Y. Ogawa[3] [iD], M. Kellinsalmi[4], T. Raita[5], A. Aikio[2] [iD], H. Vanhamäki[2] [iD], K. Shiokawa[1] [iD], I. Virtanen[2] [iD], L. Cai[6] [iD], A. B. Workayehu[2] [iD], M. Pedersen[2], K. Kauristie[4] [iD], T. T. Tsuda[7] [iD], B. Kozelov[8] [iD], A. Demekhov[8] [iD], A. Yahnin[8] [iD], F. Tsuchiya[9] [iD], A. Kumamoto[9] [iD], Y. Kasahara[10] [iD], A. Matsuoka[11], M. Shoji[1] [iD], M. Teramoto[12] [iD], and M. Lester[13] [iD]

[1]Institute for Space-Earth Environmental Research, Nagoya University, Nagoya, Japan, [2]Space Physics and Astronomy Research Unit, University of Oulu, Oulu, Finland, [3]National Institute of Polar Research, Tachikawa, Japan, [4]Finnish Meteorological Institute, Helsinki, Finland, [5]Sodankylä Geophysical Observatory, University of Oulu, Oulu, Finland, [6]Space and Plasma Physics, School of Electrical Engineering and Computer Science, KTH Royal Institute of Technology, Stockholm, Sweden, [7]Department of Computer and Network Engineering, The University of Electro-Communications, Chofu, Japan, [8]Polar Geophysical Institute, Apatity, Russia, [9]Graduate School of Science, Tohoku University, Sendai, Japan, [10]Graduate School of Natural Science and Technology, Kanazawa University, Kanazawa, Japan, [11]Kyoto University, Kyoto, Japan, [12]Department of Space Systems Engineering, Kyushu Institute of Technology, Kitakyushu, Japan, [13]Department of Physics and Astronomy, University of Leicester, Leicester, UK

Abstract Various subauroral optical features have been studied by analyzing data collected during periods of geomagnetic disturbances. Most events have been typically found at geomagnetic latitudes of 45–60°. In this study, however, we present a red arc event found at geomagnetic 68° north ($L \approx 7.1$) in the Scandinavian sector during a period of geomagnetically quiet conditions within a short intermission between two high-speed solar wind events. The red arc appeared to coincide with a pseudo breakup at geomagnetic 71–72°N and a rapid equatorward expansion of the polar cap. However, the red arc disappeared in approximately 7 min. Simultaneous measurements with the Swarm A/C satellites indicated the appearance of the red arc at the ionospheric trough minimum and a conspicuous enhancement of the electron temperature, suggesting the generation of the arc by heat flux. Since there are meaningful differences in the red arc features from already-known subauroral optical features such as the stable auroral red (SAR) arc, we considered that the red arc is a new phenomenon. We suggest that the ephemeral red arc may represent the moment of SAR arc birth associated with substorm particle injection, which is generally masked by bright dynamic aurorae.

1. Introduction

The subauroral region is aligned with but separate from the equator side of the auroral oval, and its latitude can shift equatorward (poleward) with increasing (decreasing) geomagnetic activity. The subauroral F region electron density at dusk to premidnight sector is lower than that in the auroral region, which is ionized by auroral electron precipitation from the plasma sheet. The F region electron density at the equator side of the subauroral region is maintained by plasma from the plasmasphere along the magnetic field line. The poleward side of the subauroral region is separated from the plasmasphere but is not separated from the plasma sheet. Thus, the plasmapause maps into the subauroral ionosphere along magnetic field lines.

The most prominent subauroral optical feature represented by a long academic history is the stable auroral red (SAR) arc (e.g., Cornwall et al., 1971; Inaba et al., 2020; Kozyra et al., 1997; Mendillo et al., 2016; Rees & Roble, 1975; Shiokawa et al., 2017; Takagi et al., 2018). The SAR arc is a monochromatic emission of the atomic oxygen at 630.0 nm in the F region, typically appearing at the recovery phase of storms and substorms. A possible generation mechanism is the Coulomb collision of bouncing ring current hot ions with thermal electrons mainly at the mirror point on the magnetic field line (Cole, 1965). Energized thermal electrons can transport the heat flux down to the ionosphere, and then atomic oxygen in the top ionosphere is excited to the O(^{1}D) state. The F region electron temperature occasionally has a peak in the ionospheric trough
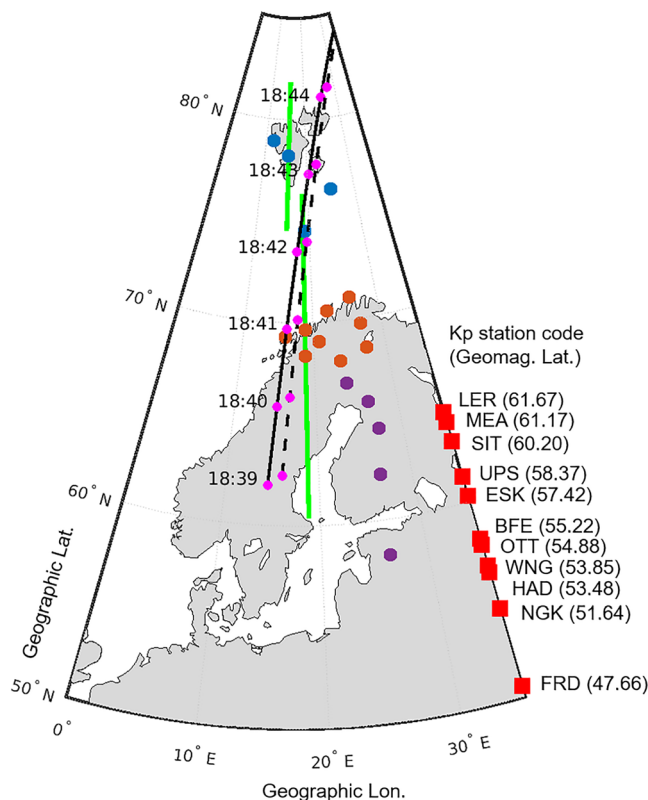
Figure 1. Solid circles in blue, orange, and purple are marked at the IMAGE magnetometer sites, which have been employed for deriving the *IU* and *IL* indices. The magnetometer sites are grouped into three areas: the Svalbard-Bear Island area (blue), northern Scandinavia (orange), and southern Scandinavia (purple). Green lines represent the area, where the keograms are composed of all-sky cameras at Longyearbyen and Abisko assuming emission heights of 110 and 210 km, respectively. Red squares are marked at the geomagnetic latitudes of the magnetometer sites, which have been adopted for deriving the *Kp* index (11 sites in the Northern Hemisphere). Solid and dashed black curves show the trajectories of Swarm A and Swarm C, respectively. Dots in magenta are marked every minute from 18:39 to 18:44 UT.

minimum (or the electron density minimum) at premidnight magnetic local time (MLT) (Prölss, 2006; Pryse et al., 1998; Rodger et al., 1992; Voiculescu et al., 2010), which is evidence of heat conduction from the inner magnetosphere. The observational evidence supports the generation of the SAR arc in the ionospheric trough by heat conduction. Foster et al. (1994) and Förster et al. (1999) concluded by analyses of storm time data that there is a close relationship between the location of the SAR arc, the electron-temperature peak, and the narrow trough with width of a few degrees in latitude. This observational result bolsters the argument that the Coulomb collision process is the SAR arc generation mechanism. On the other hand, a case study of the postmidnight trough presented no (or small) electron temperature elevations in incoherent scatter radar (ISR) measurements (Voiculescu et al., 2016), although optical data were not available for the event. The occurrence rate of the SAR arc peaks at premidnight (20–22 MLT), but events in the postmidnight sector are not rare (Takagi et al., 2018). While heat transfer can be a prevailing mechanism of SAR arc generation, the postmidnight SAR arc implies other mechanisms, which may be related to wave-particle interactions through ion cyclotron wave damping and Landau damping of kinetic Alfvén waves (Kozyra et al., 1997).

Most SAR arc events have been found during the recovery phase of storms and substorms, when the subauroral region is likely located at moderately low *L* values (2–4), corresponding to geomagnetic latitudes of 45–60° (Ievenko et al., 2008; Slater & Kleckner, 1989). While the SAR arc position moves poleward with diminishing storm activity, we do not know its poleward limit, that is, the lowest geomagnetic activity necessary to generate the SAR arc. While it has been considered that the SAR arc is a phenomenon during the recovery phase of storms and substorms as described above, we do not know whether the SAR arc would be only generated at the substorm recovery phase or if the initial development would be masked by bright auroral activities at the substorm expansion phase until the SAR arc becomes apparent on the dark trough after shrinking of the auroral oval.

This study analyzed measurements from various instruments during periods of geomagnetically quiet conditions represented by *Kp* values of 0 + but associated with a pseudo breakup. Since aurorae did not expand equatorward too much from the pseudo breakup latitude during the period corresponding to its expansion phase, we were able to find subauroral optical features associated with the pseudo breakup. After introducing the data set along with the background geomagnetic condition in section 2, the observation results of an event on 20 February 2018 will be presented in section 3. All-sky cameras (630.0 nm) captured an arc structure at the equator side of the auroral oval separated by a spatial gap. Some features were similar to the traditional SAR arc, but other features were not. Some possible mechanisms to generate the red arc will be discussed in section 4. Section 5 will summarize this study with conclusions.

2. Data Sets and the Background

In this study, integrated analyses were conducted by using measurements with multiple instruments operated in Svalbard and Fennoscandia on the ground and satellites at the dusk sector on 20 February 2018. International Monitor for Auroral Geomagnetic Effects (IMAGE) magnetometers (https://space.fmi.fi/image), which have been operated at the locations marked by solid circles in Figure 1, were grouped into three areas (Svalbard-Bear Island area [blue], northern Scandinavia [orange], and southern Scandinavia [purple]). The grouping was adopted for estimating the regional *AU* and *AL* indices in this sector (hereinafter written as *IU* and *IL*, respectively). Abisko station, which is grouped into the northern Scandinavia

(orange), is one of the AE stations. The *IU* and *IL* can detect ionospheric current variations at higher latitudes than the ordinary *AU* and *AL*. This condition means that *IU* and *IL* may be more sensitive to ionospheric current variations during periods of geomagnetically quiet conditions even if *AU* and *AL* do not show notable signatures due to the large relative distance between the current density peak and the adopted magnetometer sites. Since this study will focus on an event appearing during a geomagnetically quiet period, as discussed later in this section and in section 3, *IU* and *IL* are more appropriate than *AU* and *AL*.

Images from all-sky cameras at Longyearbyen (Norway, geographic coordinates 78.15°N, 16.03°E; 557.7 nm), Abisko (Sweden, geographic coordinates 68.36°N, 18.82°E; 557.7 and 630.0 nm), Kilpisjärvi (Finland, geographic coordinates 69.05°N, 20.78°E; 557.7 and 630.0 nm), and Lovozero (Russia, geographic 67.97°N, 35.08°E; 557.7 nm) were investigated in this study, and carefully selected images and results will be presented in the article. The camera at Longyearbyen is mounted with a low-cost Watec monochromatic sensor with an optical band-pass filter of 557.7 nm and an all-sky lens (Ogawa et al., 2020). The exposure time is 1 s. The cameras at Abisko and Kilpisjärvi belong to the Magnetometers Ionospheric Radars All-sky Cameras Large Experiment (MIRACLE) camera network (Sangalli et al., 2011). The cameras are equipped with an electron multiplying CCD (EMCCD) sensor mounted with an optical filter wheel, which holds optical band-pass filters of 557.7, 427.8, and 630.0 nm. The exposure times of the 557.7 and 630.0 nm images, which have been analyzed in this study, are 0.8 and 1.2 s, respectively. The camera at Lovozero is equipped with an EMCCD sensor and an all-sky lens. The exposure time of the 630.0 nm image is 10 s. Vertical green bars in Figure 1 are drawn along the meridional line in the field of view (FOV) of the Longyearbyen 557.7 nm camera (assumed emission height of 110 km) and that of the Abisko 630 nm camera (assumed emission height of 210 km; see Appendix A). These lines correspond to meridional sectors used to make keograms at the sites. The red squares in Figure 1 are marked at the geomagnetic latitude of individual magnetometer sites adopted for deriving the *Kp* index in order to emphasize the latitude difference between IMAGE and *Kp* stations. Solid and dashed black lines are drawn along the Swarm A and C trajectories, respectively. The time stamp is marked in magenta every minute from 18:39 to 18:44 UT. In this study, the electron density and temperature obtained with the Swarm satellites were analyzed.

Figure 2 shows the general conditions of the solar wind and geomagnetic activity for 30 days around the event time, which is marked by vertical dashed red line. For the first half of the period, 1–14 February 2018, the solar wind flow speed (panel a) remained at a slow level at ~400 km/s or lower, resulting in weak geomagnetic activity, as seen in the *SYM-H* and *Kp* indices (panels e and f, respectively), despite occasional increases in the solar wind density (panel c). However, for the second half of the period, which is highlighted by a green box, after an obvious increase in the interplanetary magnetic field (IMF) By and Bz magnitude (panel b) on 15–16 February, high-speed solar wind (HSSW) reached the earth peaking quasiperiodically on 19, 23, and 27 February with intervals of several days. Coinciding with the first HSSW arrival, the geomagnetic activity increased as recognized by negative deviations of *SYM-H* having moderately small magnitudes at approximately 20 nT. The *Kp* index varied and roughly synchronized with the HSSWs. To find the plasmapause location, the plasma density was inferred from the upper hybrid resonance frequency derived from the High Frequency Analyzer (HFA) (Kumamoto et al., 2018), which is a subcomponent of the Plasma Wave Experiment (PWE) (Kasahara et al., 2018) onboard the Exploration of Energization and Radiation in Geospace (ERG or "Arase") satellite (Miyoshi, Shinohara, et al., 2018), along with the magnetic field data measured with the Magnetic Field Experiment (MGF) instrument (Matsuoka et al., 2018). In this study, the plasmapause was identified as a sharp density drop by a factor of 5 or larger within an *L* value of 0.5 (Carpenter & Anderson, 1992). For the first half of the period, the estimated plasmapause location, which is represented by the magnetic latitude mapped down to 300 km height along the local magnetic field line, stayed at approximately 65 MLat (panel d). However, after the arrival of the HSSW, the plasmapause occasionally shifted inward or toward low latitudes. Quasiperiodic variations in the plasmapause location appeared to be synchronous with the HSSW and *Kp* index. At the event time (marked by a dashed red line at 18–19 UT on 20 February 2018), the plasmapause experienced a transition from the compressed to a relaxed configuration, although there might have been a dawn-dusk asymmetry of the plasmasphere. The event to be presented in this study was found between the first and the second HSSW events, and the *Kp* index was 0+. The latter fact indicates that even though the event interval can be categorized into geomagnetically quiet conditions, it might be better described as a short intermittence of magnetospheric disturbances between the two HSSWs.
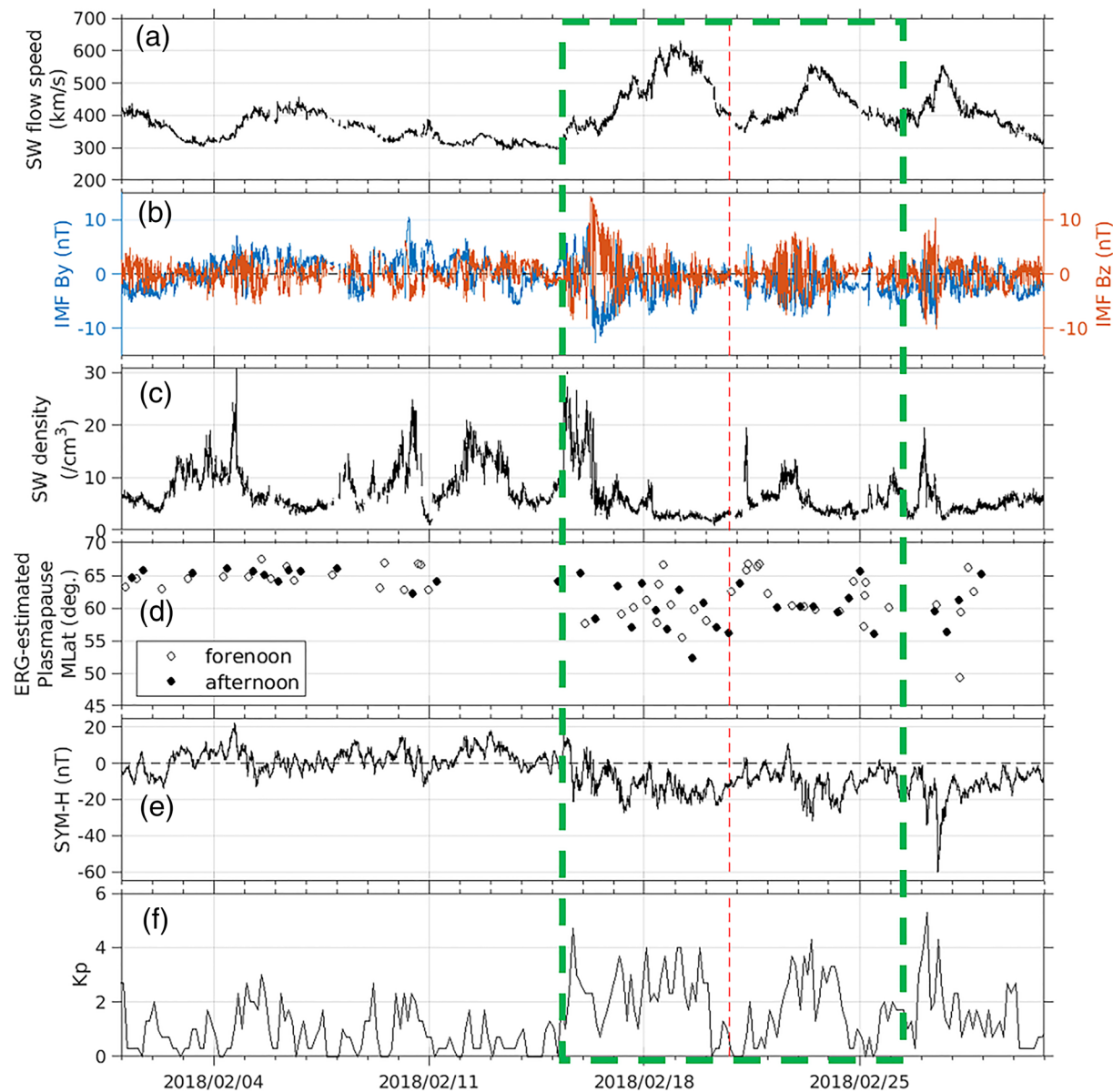
Figure 2. Variations in (a) solar wind flow speed, (b) IMF By (blue) and Bz (orange) components in the GSM coordinate, (c) solar wind density, (d) magnetic latitude of the plasmapause estimated from ERG satellite measurements at forenoon (0–12 MLT; open circle) and afternoon (12–24 MLT; solid circle), (e) *SYM-H*, and (f) *Kp* index for 30 days from 1 February to 2 March 2018. Vertical dashed red lines are marked at the event time (18:40 UT on 20 February 2018), and a green box is marked to highlight the period of interest.

3. Observations on 20 February 2018

3.1. Ground-Based Measurements

Figure 3 presents snapshots of the Abisko camera images to be discussed in this study. All of the 630 nm images were mapped on the geographical coordinates under the assumption of 210 km emission height which was derived by searching for the best match of two images taken at Abisko and Kilpisjärvi and adjusting to the assumed height (see Appendix A). The bright area spreading at the top is part of the main auroral oval. At 18:39:35 UT, near the auroral oval but at the east edge of the FOV, a narrow bright strip can be observed. One may find an indication of the strip even in the image at 18:38:35 UT. The strip extended westward until at least 18:42:35 UT, thus lasting for 4 min. The westward extension can be more clearly seen in the supporting information Movie (S1). Auroral brightening was also identified in the images taken at Lovozero (approximately 665 km eastward of Abisko) but behind thin clouds (not shown here). A few
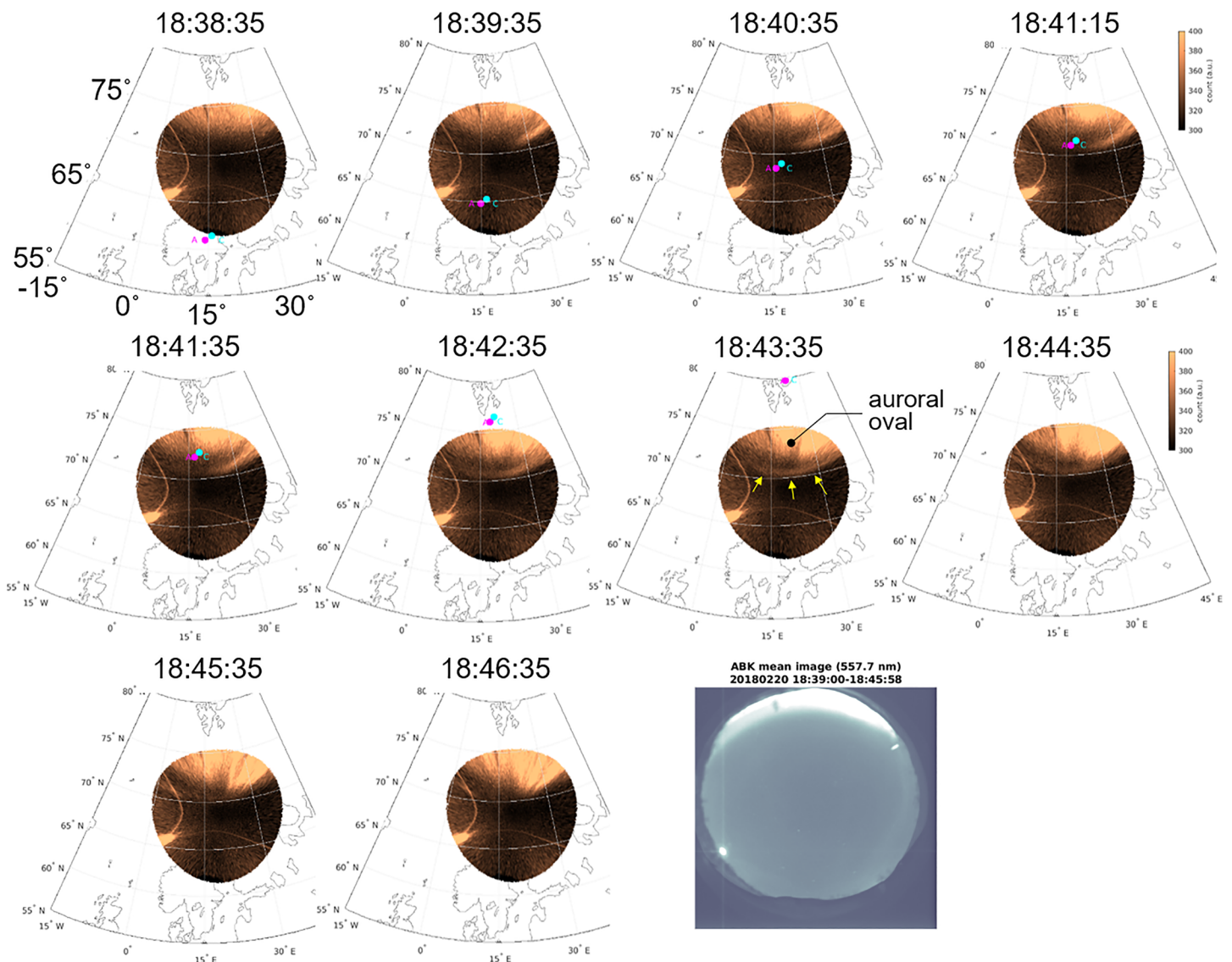
Figure 3. (First 10 images) All-sky images (630 nm) taken at Abisko, Sweden, from 18:38:35 to 18:46:35 UT on 20 February 2018. The images are mapped at the geographical coordinates assuming an emission height of 210 km. Reference lines are drawn at 55–80° every 5° for latitude and at −15 to +45° every 15° for longitude. The locations of Swarm A and Swarm C at corresponding image times are marked by magenta and cyan dots, respectively, but shifted in the mapping procedure (see the text). A bright spot at the left and a couple of antenna-like curves are moonlight reflections. In the image taken at 18:43:35 UT, the auroral oval and the red arc are highlighted by a black dot and yellow arrows, respectively. (Last image) All-sky image (557.7 nm) from the same camera after calculating the average from 18:39:00 to 18:45:58 UT. A dark crack near the top north but slightly west side is a shadow of a tree. Moonlight reflections can be seen at the southwest and northeast edges.

minutes before the start of the westward extension, the video shows a few bright patches drifting westward inside of the auroral oval. Then, at the east side of the westward drifting patches, a few bright blobs gushed out, and those structures appeared to drift slightly eastward. From one of the eastward drifting blobs, the arc structure developed and extended westward with time. Taking into account this temporal evolution, protrusion may be a more appropriate expression than detachment, which seems to be frequently cited for presenting the relative configuration between the main auroral oval and subauroral optical features such as the SAR arc and isolated proton aurora (Burch et al., 2002; Immel et al., 2002; Sakaguchi et al., 2008; Shiokawa et al., 2017; Spasojević et al., 2004; Takagi et al., 2018; Zhang et al., 2005). Between 18:42:35 and 18:43:35 UT, the arc did not transform apparently, but for the next 2 min (18:44:35 to 18:45:35 UT), the arc luminosity decreased but remained still visible. At 18:46:35 UT, it was difficult to identify the arc structure in the image. Thus, the red arc was detectable for 7 min in total (from 18:38:35

to 18:45:35 UT). The last panel in the gray color scale presents an all-sky image taken with the same camera at Abisko through an optical filter of 557.7 nm. Except for a bright auroral band zonally aligned to the northern edge of the FOV, there is no other visible optical signature capable of colligating the arc structure seen in the 630.0 nm images.

During this short emergence of the red arc, Swarm A (magenta dot) and Swarm C (cyan dot) crossed the arc almost perpendicularly at 18:41 UT. In Figure 3, the mapped location of the spacecraft was displaced horizontally by taking into account the dip angle of the magnetic field line and vertical difference between the 630 nm emission height (210 km) and the Swarm trajectory (at 435 km height). The measurements will be illustrated later (in Figure 6).

Figure 4 was created using integrated data from ground-based instruments operated in the northern Scandinavian area from 18 to 19 UT on 20 February 2018. The *IU* index at the most northern part (blue curve in Figure 4a; see also Figure 1 to identify the magnetometer sites) showed weak but positive deviations by 18:33 UT; then, the *IL* and *IU* indices at the poleward side (both in blue) became negative. These trends can typically be seen around the substorm onset along with the ionospheric current turning from eastward to westward, although magnetic field deviations are usually much larger than this event. Since the *IL* index at the two other areas was considerably less negative than the value at the most poleward area, it is considered that the ionospheric current density peaked at near the Svalbard-Bear Island area. As a reference, the Special Sensor Ultraviolet Spectrographic Imager (SSUSI) instrument onboard Defense Meteorological Satellite Program (DMSP) F17 (orbit number: 58293) showed a narrow auroral oval located south of the Svalbard Islands (not shown here).

Two keograms that were created from images captured by the cameras at Longyearbyen (Figure 4c) and Abisko (Figure 4d) show sudden brightening slightly after the negative turning of the *IU* and *IL* indices. These features suggest an auroral breakup despite considerably small variations in the magnetic field and their occurrence at high latitudes. Therefore, in this article, we refer to this auroral brightening with magnetic variations as a "pseudo breakup" (Partamies et al., 2003). Since these auroral signatures were captured near the horizon of each camera FOV, the mapping process might have caused ambiguity to be reckoned with. However, the auroral behavior looks identical in both keograms (note that apparent differences in latitudinal distribution may be artifacts attributed to vertical distributions of the emission intensity, which have resulted in poleward and equatorward illusion in the mapping procedure applied on equatorward and poleward looking line of sight, respectively). Before the pseudo breakup, aurorae appeared at 74–76°N and then expanded mainly poleward. Figure 4e shows a keogram created from the 630 nm images taken at Abisko. As highlighted by yellow arrows in the panel, the arc, which is also shown in Figure 3, has been reproduced as the vague outline of a blob but spatially separated from the main auroral oval. While it would be difficult to extract the meridional motion in Figure 3 and Movie S1, in Figure 4e the equatorward drift from 72–73° to 70°N can be observed. Figure 4f presents the cross polar cap potential (PCP) estimated from the Super Dual Auroral Radar Network (SuperDARN) measurement. Of particular interest is the synchronization of the appearance and disappearance of the red arc with a sudden increase and decrease in the cross PCP soon after the pseudo breakup. The coincidence may provide insight into red arc generation, as discussed in section 4.1.

3.2. Satellite Measurements

This event occurred during geomagnetically quiet conditions ($Kp = 0+$), which occurred for a calm interval between two HSSWs peaking on 19 and 23 February (Figure 2). The plasmasphere had not yet been completely refilled to the previous quiet level (Figure 2d). Figure 5 shows the IMF measured with the ACE satellite (time shift of 0.907 hr taking into account the solar wind speed and the distance from the satellite position to the dayside front of the magnetopause, which was identified with the Magnetospheric Multiscale (MMS) measurements (not shown here)). The total magnetic field (panel a) increased by 0.2–0.3 nT at 18:15–18:25 and 18:43–18:48 UT. At the second interval, the magnitude decreased by 0.1–0.2 nT for a few minutes before successive increase. The appearance of the red arc, from 18:38 to 18:45 UT as marked by a red bar in Figure 5, almost synchronizes with variations for the second interval, although there may be a time lag probably because of the rippled surface of the magnetopause as seen in MMS measurements. The variations are mainly attributed to the X component (toward Earth, blue curve in panel b), and the solar wind could have impacted the magnetopause. The IMF Bz component had remained negative for
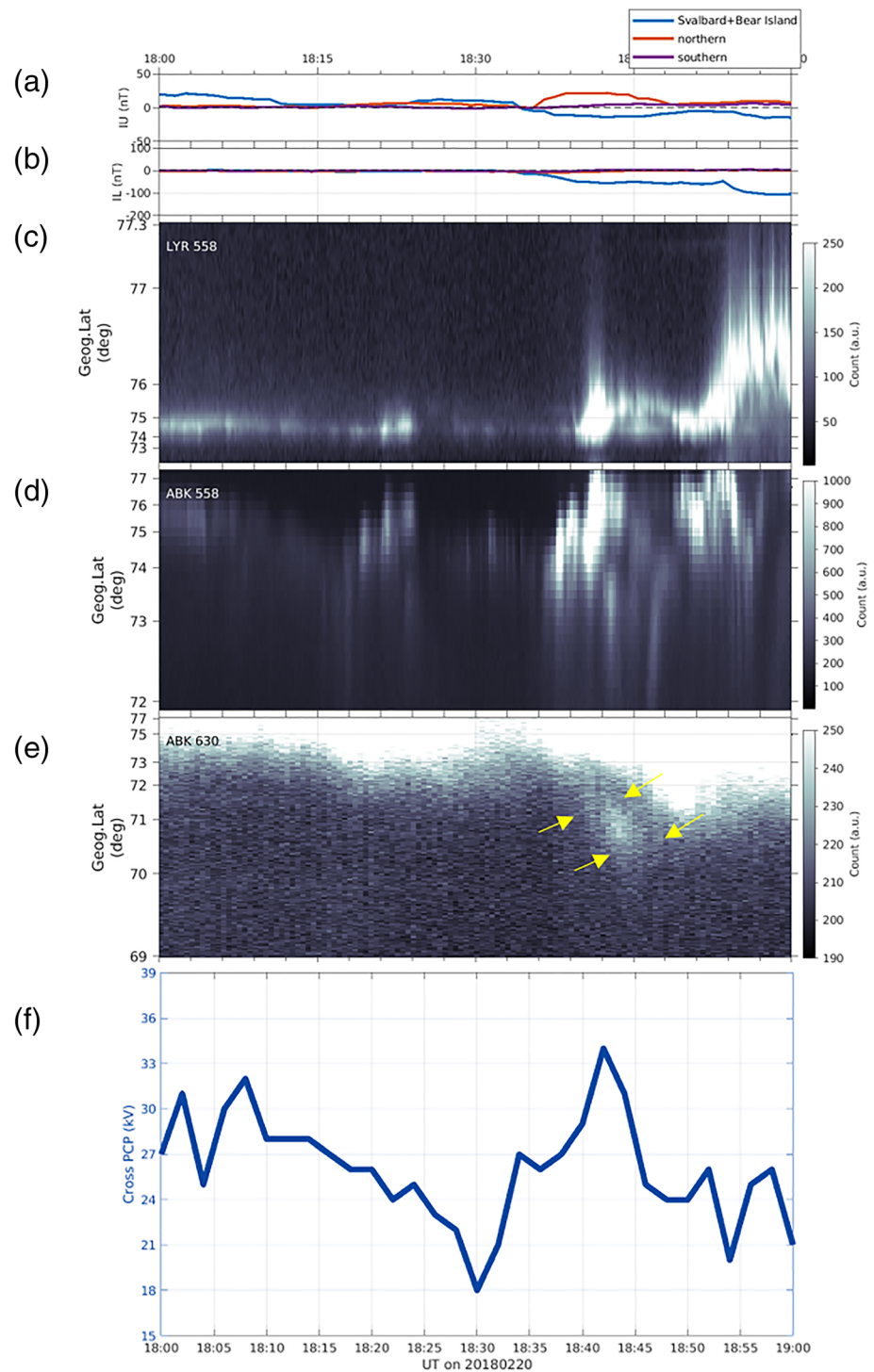
Figure 4. Time series of (a, b) *IU* and *IL* indices derived from the IMAGE magnetometer measurements but grouped into the three areas (blue: Svalbard and Bear Island; orange: northern Scandinavia; purple: southern Scandinavia), (c, d) keogram created from all-sky images (557.7 nm) taken at Longyearbyen and Abisko, (e) keogram created from all-sky images (630.0 nm) taken at Abisko, and (f) cross polar cap potential in kV estimated by the SuperDARN measurements. All panels show measurements at 18–19 UT on 20 February 2018.

Figure 5. Temporal variations in the (a) total magnetic field and (b) three components of the magnetic field (in the GSM coordinate) measured with the ACE satellite. The time stamp was shifted by 0.907 hr by assuming dayside magnetopause at 11 Re, which was estimated by the MMS measurement. The time interval of the appearance of the ephemeral red arc is highlighted by red bars (from 18:38 to 18:45 UT).
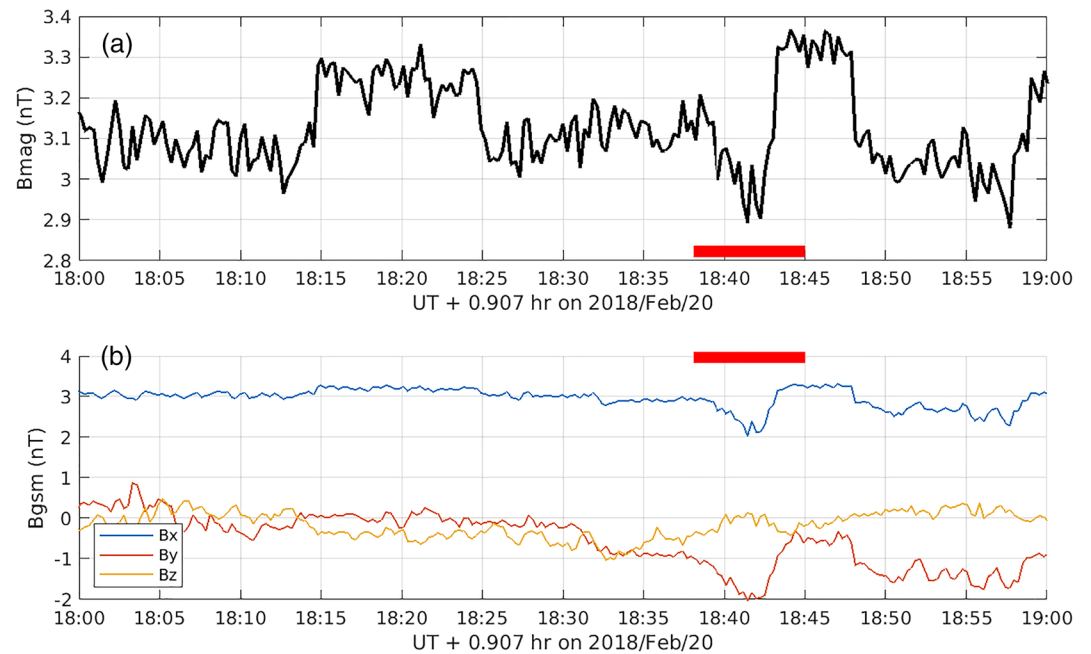
approximately 30 min before the appearance of the red arc. These IMF situations may cause the generation of the pseudo breakup and the red arc.

As presented in Figure 3, during the red arc appearance, Swarm A and Swarm C crossed the arc almost perpendicularly at 18:41 UT. Figure 6 presents the latitudinal profiles of the Swarm measurements of the electron density (curves in cold hue) and the electron temperature (curves in warm hue). Measurements of Swarm A and Swarm C are illustrated in individual light and dark colors, respectively. As discussed in Appendix A, the red arc emission height has been estimated as 210 km with an intensity peak at 71°N when the locations of Swarm A and Swarm C are closest to the red arc (see Figure A1). This result means that Swarm measurements at 71°N denote the ionospheric condition inside of the red arc. The latitude at the
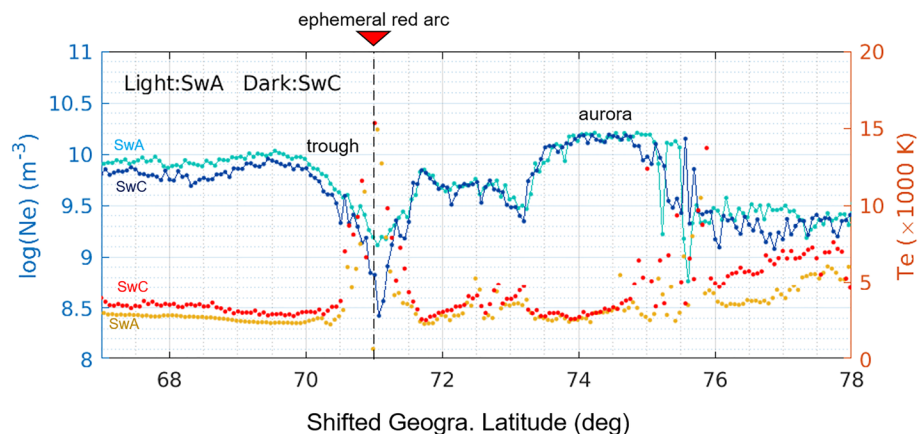
Figure 6. Electron density and temperature (cold and warm hues, respectively) measured with the Swarm A (lighter color) and Swarm C (darker color) satellites. The estimated location of the ephemeral red arc is marked by a red triangle and a dashed line (see Figure A1). Latitude at the swarm measurement was shifted by 0.48–0.28° (dependent on latitudes at 67–78°N) to poleward while being mapped down along the magnetic field line from the operation altitude of 435 km to the estimated emission height of 210 km (see Appendix A).

Swarm measurement was shifted poleward by 0.48–0.28° (dependent on latitudes at 67–78°N) in Figure 6 while being mapped along the magnetic field line from the operation altitude of 435 km to the estimated emission height. The Swarm measurements show a clear density depression, which is a feature of the iono-spheric trough, at 70.0–71.7°N along with high electron temperature, which reaches ~15000 K at the trough minimum at ~71°N. There are some differences in the electron density at the trough minimum between the two spacecraft but almost no difference in the electron temperature. As illustrated by the vertical dashed line in Figure 6, the red arc was located at the trough minimum with high electron temperature. The electron temperature was measured with the Langmuir probe, and the amplitude of the temperature ambiguity would be 10% or slightly larger (Siefring et al., 1998). Considering a higher-energy part of the electron distri-bution function for the measured temperature of ~15000 K, some electrons would be heated to energies greater than 1.959 eV (22732 K), which is the energy necessary to excite atomic oxygen to the $O(^1D)$ state from the ground state. However, dissociative recombination production of $O(^1D)$ may not require such a high energy. The 630 nm emission could reach many kR for electron temperatures higher than 4000 K (Carlson et al., 2013; Kozyra et al., 1990). It is therefore reasonable to assume that substantial heat flux was transferred into the ionosphere to generate the ephemeral red arc.

4. Discussion

4.1. Possible Generation Mechanism

We presume that the scenario including the heat conduction that caused the observed electron temperature maximum and the ephemeral red arc is the same as the prevailing mechanism that generated the SAR arc, as mentioned in section 1. While the SAR arc has been found at the substorm recovery phase, its signature at the expansion phase, if any, would have been hidden because of the preponderantly bright aurora. Since pre-vious subauroral observations at the substorm growth phase have shown no signs of the SAR arc, the SAR arc should be generated between the substorm onset and the beginning of the recovery phase. We need more studies to confirm this supposition, but the red arc in this study may represent a moment of SAR arc birth after the substorm onset, although the red arc for this event did not grow to a persistent red arc, probably due to a short-lived satisfaction of the red arc generation. The heat flux that creates the SAR arc is caused by Coulomb collision between ring current ions and plasmaspheric electrons (e.g., Kozyra et al., 1987). The overlap of these two plasma populations occurs during the recovery phase of the storm due to refilling of the plasmasphere. However, similar overlap can occur due to inward injection of ring current ions asso-ciated with substorms, as suggested by Shiokawa et al. (2013). The present event may also indicate a similar mechanism of Coulomb collision between the expanded plasmasphere during this quiet interval and the ring current ions associated with pseudo breakup. However, we need to accumulate more evidence to sub-stantiate the role of the Coulomb collision process in the red arc generation. The ERG measurement signifies a discrepancy between the plasmapause MLat (56.2° at 17:30 UT, i.e., 15:07 MLT and 62.5° at 20:10 UT, i.e., 8:42 MLT on 20 February 2018) and the red arc MLat (68°) (see Figure 2d). The hull of the plasmasphere should be embedded in the ring current region to manifest the Coulomb collision process. However, the MLat discrepancy suggests difficulty in meeting the situation. On the other hand, it is possible to consider an azimuthally asymmetric evening sector enhancement in plasma density as the reason of discrepancy. Since the ERG measurement was conducted far from the Scandinavian sector for the period, observational substantiation using magnetospheric satellites is a future work.

As summarized in Table A1, the 630 nm emission height was estimated from 18:40:35 to 18:44:35 UT. Focusing on the lowest height at each time, the first two and the last events (i.e., 18:40:35, 18:41:15, and 18:44:35) have lower bounds at 180–200 km, while the other three are tens of kilometers lower at 130–170 km. However, for all the cases, the highest emission height seems to be more stable at approxi-mately 200 km and is separated from the last case. Triangulation from two meridional scanning photometer stations showed the best fitted emission height of the SAR arc in the range of 370–460 km (Okano & Kim, 1987). A 630 nm emission height of 230–240 km may have been adopted as a standard height in the literature. However, this height was derived based on an airglow study (Blanchard et al., 1997). A triangula-tion method, which was applied on the red line discrete arc, derived the best auroral mapping at 180–220 km in altitude (Jackel et al., 2003). A comparison of the field-aligned current (FAC) location identified with the Swarm satellites with the red auroral arcs measured with all-sky cameras suggested a characteristic emission height of 200 km (Gillies et al., 2017). Red line emission is not frequently observed below 150 km

Table 1
General Characteristics of the SAR Arc, STEVE, and the Ephemeral Red Arc Found in This Study

	SAR arc	STEVE	Ephemeral red arc
Appearance	During the storm and substorm recovery phase with stable long lifetime	During the storm time substorm recovery phase	Appearance at pseudo breakup during a minor storm (min. *SYM-H* of −20 nT) for a short interval (7 min)
Emission	Spectrally pure 630.0 nm emission peaking at ~400 km altitude	Multiple emissions including purple/mauve colors	Found in the red (630.0 nm) emission peaking at ~210 km altitude but not in the green (557.7 nm) one
Morphology	Zonally long structure aligned the trough minimum with high electron temperature	Zonally elongated in association with the picket fence structure at the green line and westward drift	Zonally elongated at the trough minimum with high electron temperature, growing westward

(Eather, 1969), probably due to suppression of O(^{1}D) by the atmospheric quenching process. Compared with these previous works, the estimated height of 210 km may be acceptable, but that of 130–170 km appears to be close to the lowest limit or even lower.

The estimated red arc height is apparently lower than the SAR arc height (~400 km) estimated in previous studies. This difference may suggest that electron precipitation at an energy of hundreds of electronvolts, which can penetrate to 210 km, excites atomic oxygen along with heat conduction. A SAR arc measurement in conjunction with the Van Allen Probes showed that parallel electron precipitation was produced by strong Alfvén waves at the plasmapause (Chu et al., 2019). Future simultaneous measurements of the height-resolved electron density and temperature with the ISR may give a new insight to evaluate relative importance between the soft electron precipitation and the heat flux.

While the electron temperature measurement at the trough minimum was almost identical between Swarm A and Swarm C, the Swarm A electron density was higher than Swarm C value by approximately 5 times (see Figure 6). Swarm A flew in the west side of the Swarm C by approximately 57 km and crossed same latitude as the Swarm C 8 s later. Higher Swarm A density at the equator side of the trough may be attributed to the zonal gradient from the dusk solar terminator. However, there should be other mechanisms to generate larger differences in the trough. The recombination rate of the O$^+$ density is unresponsive to the electron temperature increase but strongly dependent on the ion temperature at 400 km level (Watkins, 1978). High electron temperature in the trough would not be the causality to produce the difference of the electron density. It is thus conjectured that the ion temperature or the electric field might have spatial and/or temporal fine structures in the trough, although it is out of scope of this study.

An unconfined broad range of meridional thickness of the red line emission could cause a challenge in the projection procedure. In the case of an arc located at the polar side of the observer, poleward broadening is equivalent to downward broadening in the projection procedure. This ambiguity may have resulted in noticeably low emission heights from estimation.

4.2. SAR Arc, STEVE, or a New Type?

In addition to the SAR arc, several subauroral optical features have been reported, for instance, afternoon detached proton arcs (Burch et al., 2002; Immel et al., 2002; Spasojević et al., 2004), subauroral morning proton spots (SAMPS; Frey et al., 2004), nightside detached aurora (NDA; Zhang et al., 2005), isolated proton aurora (e.g., Sakaguchi et al., 2008; Søraas et al., 2013), and strong thermal emission velocity enhancement (STEVE) and its associated picket fence (Chu et al., 2019; Gallardo-Lacourt et al., 2018; MacDonald et al., 2018; Nishimura et al., 2019). The most notable difference of the red arc event in this study from these previous results is the geomagnetic conditions and geomagnetic latitude of its emergence. While all events in the previous works were found in measurements during considerably active conditions such as storms and substorms, the *Kp* index of the red arc event in this study was 0+. The auroral oval was thus shrunk poleward up to 71–72° MLat, and the red arc appeared at 68° MLat ($L \approx 7.1$), which is a considerably high latitude never reported in the previous subauroral optical features.

Another notable difference is the phase relative to the onset of auroral brightening. The SAR arc, detached/isolated aurora, and STEVE have been found at the storm and substorm recovery phase, but the ephemeral
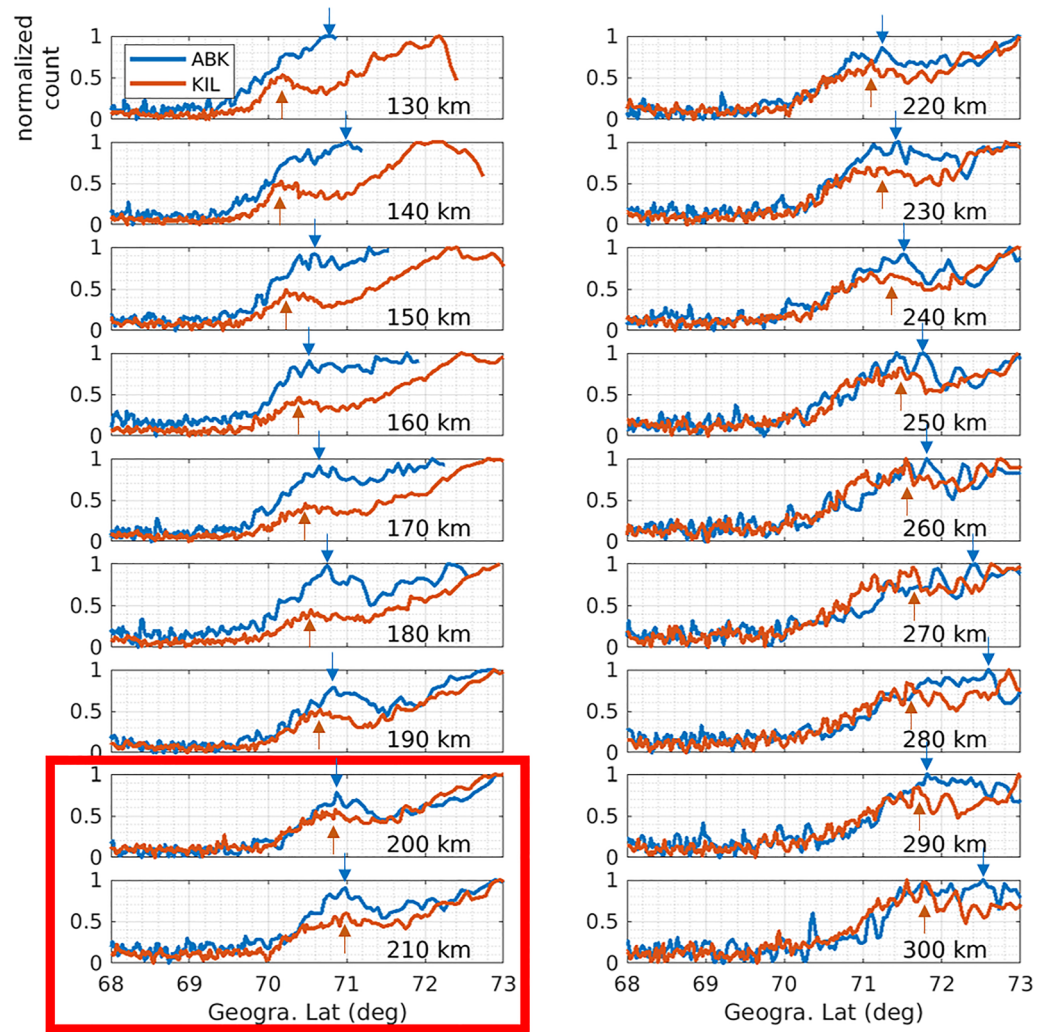
Figure A1. Latitudinal features of the camera count taken at Abisko (blue) and Kilpisjärvi (orange) at 23.0–23.2°E at 18:41:15 UT on 20 February 2018 under the assumption of a 630 nm emission height of 130–300 km (numbers in each panel). The image count was normalized by the maximum between 68°N and 73°N. The estimated red arc locations in the Abisko and Kilpisjärvi images are marked by arrows in individual colors. A red square highlights two cases, in which the location of the red arc in the Abisko images agrees with that in the Kilpisjärvi images.

red arc in this study coincided with a pseudo breakup. Furthermore, the duration of this event was much shorter (7 min) than that of other events, which could last for hours. Table 1 examines the resemblance between the SAR arc, STEVE, and the ephemeral red arc in this study. It is concluded that the ephemeral red arc cannot be clearly categorized into either of the other two, so it must be an event that has not yet been reported.

5. Summary and Conclusions

An ephemeral red arc in this study was observed at high latitude in the evening sector during the period of geomagnetically quiet conditions characterized by $Kp = 0+$ but coincided with a pseudo breakup. The event had different features from other subauroral optical phenomena, the SAR arc, and the STEVE. As far as we know, this kind of red arc has never been reported in the literature. A notable feature is the high geomagnetic latitude of appearance at MLat 68°N or $L \approx 7.1$. The comparison of camera images and Swarm measurements revealed that the ephemeral red arc emerged at the trough minimum with a high electron temperature of ~15000 K. SuperDARN and ACE measurements suggested that quasiperiodic oscillations

Table A1
Estimated 630 nm Emission Height From 18:40:35 to 18:44:35 UT

UT	Estimated height (km)	Center height and width (km)
18:40:35	180–210	195 ± 15
18:41:15	200–210	205 ± 5
18:41:35	130–200	165 ± 35
18:42:35	150–210	180 ± 30
18:43:35	170–190	180 ± 10
18:44:35	200–230	215 ± 15

of the IMF with negative Bz for 30 min impacted the dayside magnetopause, and then a corresponding sudden increase of the cross PCP induced the ephemeral red arc. The IMF impact and the consequent cross PCP enhancement finished shortly thereafter, and the red arc also disappeared at the same time. The coexistence of the red arc with the electron-temperature peak localized at the trough minimum suggested that the heat flux transferred from the plasmapause would be the principal mechanism of red arc generation. The ephemeral red arc may represent a moment of SAR arc birth, which is generally masked by bright dynamic aurorae.

Appendix A: Estimation of the 630 nm Emission Height

Estimation of the emission height of 630.0 nm was made by comparing the two images taken at Abisko and Kilpisjärvi at the same time from 18:40:35 to 18:44:35 UT on 20 February 2018. A comparison was made between the latitudinal features of the camera image count along a longitude across the ephemeral red arc. Figure A1 is a case of images taken at 18:41:15 UT when the Swarm A and C locations were closest to the red arc, as shown in Figure 3. The image count was normalized by the maximum between 68° and 73°N. The 630 nm emission height was scanned from 130 to 300 km every 10 km, which showed that the estimated location of the red arc in the Abisko image exhibited good agreement with that in the Kilpisjärvi image in the cases of 200 and 210 km. Other optical features in 630-nm images except for the red arc may be characterized by different emission heights. However, to make Figures 3, 4e, and 6, a height of 210 km was adopted through the analyses.

Table A1 summarizes the emission heights estimated from 6 pairs of images from 18:40:35 to 18:44:35 UT. As shown in Figure 3, the ephemeral red arc can be identified before and after this selected time interval. However, a comparison study has not been conducted because the red arc in Kilpisjärvi before 18:40:35 UT has been masked by an obstacle in front of the optical dome and the red arc after 18:44:35 UT is too dim to estimate the emission height, although it is certain that the red arc is still present.

Data Availability Statement

All-sky camera images at Abisko, Kilpisjärvi, Longyearbyen, and Lovozero were obtained from individual PIs (Sodankylä Geophysical Observatory, Finland; Finnish Meteorological Institute, Finland; National Institute of Polar Research, Japan; and Polar Geophysical Institute, Russia) after checking the quick looks at their websites (space.fmi.fi/MIRACLE/ASC/, pc115.seg20.nipr.ac.jp/www/opt/lyr.html, pgi.ru/kagin/eng/). SuperDARN map potential data were obtained from its website (vt.superdarn.org/tiki-index.php?page=ASCIIData). The DMSP SSUSI, Swarm, and ACE data were obtained through their websites (ssusi.jhuapl.edu/gal_edr-aur_cs, swarm-diss.eo.esa.int, www.srl.caltech.edu/ACE/ASC/level2/). The MMS quick looks were obtained through their websites (lasp.colorado.edu/mms/sdc/public/). Access and processing data of the solar wind and geomagnetic indices were obtained using SPEDAS V3.0 through spdf.gsfc.nasa.gov/pub/data/. Science data of the ERG (Arase) satellite were obtained from the ERG Science Center operated by ISAS/JAXA and ISEE/Nagoya University (https://ergsc.isee.nagoya-u.ac.jp/index.shtml.en, Miyoshi, Hori, et al., 2018). The present study analyzed PWE-HFA L2 v01_01, MGF-L2 v03_03 data, and OBT L3 v02 data.

References

Blanchard, G., Lyons, L., & Samson, J. (1997). Accuracy of using 6300 A auroral emission to identify the magnetic separatrix on the nightside of Earth. *Journal of Geophysical Research*, *102*(A5), 9697–9703. https://doi.org/10.1029/96JA04000

Burch, J. L., Lewis, W. S., Immel, T. J., Anderson, P. C., Frey, H. U., Fuselier, S. A., et al. (2002). Interplanetary magnetic field control of afternoon-sector detached proton auroral arcs. *Journal of Geophysical Research*, *107*(A9), 1251. https://doi.org/10.1029/2001JA007554

Carlson, H. C., Oksavik, K., & Moen, J. I. (2013). Thermally excited 630.0nm O(1D) emission in the cusp: A frequent high-altitude transient signature. *Journal of Geophysical Research: Space Physics*, *118*, 5842–5852. https://doi.org/10.1002/jgra.50516

Carpenter, D., & Anderson, R. (1992). An ISEE/whistler model of equatorial electron density in the magnetosphere. *Journal of Geophysical Research*, *97*(A2), 1097–1108. https://doi.org/10.1029/91JA01548

Chu, X., Malaspina, D., Gallardo-Lacourt, B., Liang, J., Andersson, L., Ma, Q., et al. (2019). Identifying STEVE's magnetospheric driver using conjugate observations in the magnetosphere and on the ground. *Geophysical Research Letters*, *46*, 12,665–12,674. https://doi.org/10.1029/2019GL082789

Cole, K. D. (1965). Stable auroral red arcs, sinks for energy of Dst main phase. *Journal of Geophysical Research*, *70*(7), 1689–1706. https://doi.org/10.1029/JZ070i007p01689

Cornwall, J. M., Coroniti, F. V., & Thorne, R. M. (1971). Unified theory of SAR arc formation at the plasmapause. *Journal of Geophysical Research*, *76*(19), 4428–4445. https://doi.org/10.1029/JA076i019p04428

Eather, R. H. (1969). Short-period auroral pulsations in λ6300 O I. *Journal of Geophysical Research*, *74*(21), 4998–5004. https://doi.org/10.1029/JA074i021p04998

Förster, M., Foster, J. C., Smilauer, J., Kudela, K., & Mikhailov, A. V. (1999). Simultaneous measurements from the Millstone Hill radar and the active satellite during the SAID/SAR arc event of the March 1990 CEDAR storm. *Annales de Geophysique*, *17*(3), 389–404. https://doi.org/10.1007/s00585-999-0389-6

Foster, J. C., Buonsanto, M. J., Mendillo, M., Nottingham, D., Rich, F. J., & Denig, W. (1994). Coordinated stable auroral red arc observations: Relationship to plasma convection. *Journal of Geophysical Research*, *99*, 11,429–11,439.

Frey, H. U., Haerendel, G., Mende, S. B., Forrester, W. T., Immel, T. J., & Østgaard, N. (2004). Subauroral morning proton spots (SAMPS) as a result of plasmapause-ring-current interaction. *Journal of Geophysical Research*, *109*, A10305. https://doi.org/10.1029/2004JA010516

Gallardo-Lacourt, B., Nishimura, Y., Donovan, E., Gillies, D. M., Perry, G. W., Archer, W. E., et al. (2018). A statistical analysis of STEVE. *Journal of Geophysical Research: Space Physics*, *123*, 9893–9905. https://doi.org/10.1029/2018JA025368

Gillies, D. M., Knudsen, D., Donovan, E., Jackel, B., Gillies, R., & Spanswick, E. (2017). Identifying the 630 nm auroral arc emission height: A comparison of the triangulation, FAC profile, and electron density methods. *Journal of Geophysical Research: Space Physics*, *122*, 8181–8197. https://doi.org/10.1002/2016JA023758

Ievenko, I. B., Parnikov, S. G., & Alexeyev, V. N. (2008). Relationship of the diffuse aurora and SAR arc dynamics to substorms and storms. *Advances in Space Research*, *41*(8), 1252–1260. https://doi.org/10.1016/j.asr.2007.07.030

Immel, T. J., Mende, S. B., Frey, H. U., Peticolas, L. M., Carlson, C. W., Gerard, J., et al. (2002). Precipitation of auroral protons in detached arcs. *Geophysical Research Letters*, *29*(11), 1519. https://doi.org/10.1029/2001GL013847

Inaba, Y., Shiokawa, K., Oyama, S., Otsuka, Y., Oksanen, A., Shinbori, A., et al. (2020). Plasma and field observations in the magnetospheric source region of a stable auroral red (SAR) arc by the Arase satellite on 28 March 2017. *Journal of Geophysical Research: Space Physics*, *125*. https://doi.org/10.1029/2020JA028068

Jackel, B. J., Creutzberg, F., Donovan, E. F., & Cogger, L. L. (2003). Triangulation of auroral red-line emission heights. In K. U. Kaila, J. R. T. Jussila, H. Holma (Eds.), *Proceedings of the 28th annual European meeting on atmospheric studies by optical methods* (pp. 97–100). Oulu, Finland: Sodankyla Geophys. Observ. Publ.

Kasahara, Y., Kasaba, Y., Kojima, H., Yagitani, S., Ishisaka, K., Kumamoto, A., et al. (2018). The plasma wave experiment (PWE) on board the Arase (ERG) satellite. *Earth, Planets and Space*, *70*(1), 86. https://doi.org/10.1186/s40623-018-0842-4

Kozyra, J., Nagy, A., & Slater, D. (1997). High-altitude energy source(s) for stable auroral red arcs. *Reviews of Geophysics*, *35*(2), 155–190. https://doi.org/10.1029/96RG03194

Kozyra, J. U., Shelley, E. G., Comfort, R. H., Brace, L. H., Cravens, T. E., & Nagy, A. F. (1987). The role of ring current O+ in the formation of stable auroral red arcs. *Journal of Geophysical Research*, *92*(A7), 7487–7502. https://doi.org/10.1029/JA092iA07p07487

Kozyra, J. U., Valladares, C. E., Carlson, H. C., Buonsanto, M. J., & Slater, D. W. (1990). A theoretical study of the seasonal and solar cycle variations of stable aurora red arcs. *Journal of Geophysical Research*, *95*(A8), 12,219–12,234. https://doi.org/10.1029/JA095iA08p12219

Kumamoto, A., Tsuchiya, F., Kasahara, Y., Kasaba, Y., Kojima, H., Yagitani, S., et al. (2018). High frequency analyzer (HFA) of plasma wave experiment (PWE) onboard the Arase spacecraft. *Earth, Planets and Space*, *70*(1), 82. https://doi.org/10.1186/s40623-018-0854-0

MacDonald, E. A., Donovan, E., Nishimura, Y., Case, N. A., Gillies, D. M., Gallardo-Lacourt, B., et al. (2018). New science in plain sight: Citizen scientists lead to discovery of optical structure in the upper atmosphere. *Science Advances*, *4*(3), eaaq0030. https://doi.org/10.1126/sciadv.aaq0030

Matsuoka, A., Teramoto, M., Nomura, R., Nosé, M., Fujimoto, A., Tanaka, Y., et al. (2018). The ARASE (ERG) magnetic field investigation. *Earth, Planets and Space*, *70*(1), 43. https://doi.org/10.1186/s40623-018-0800-1

Mendillo, M., Baumgardner, J., & Wroten, J. (2016). SAR arcs we have seen: Evidence for variability in stable auroral red arcs. *Journal of Geophysical Research: Space Physics*, *121*, 245–262. https://doi.org/10.1002/2015JA021722

Miyoshi, Y., Hori, T., Shoji, M., Teramoto, M., Chang, T., Segawa, T., et al. (2018). The ERG science center. *Earth, Planets and Space*, *70*(1), 96. https://doi.org/10.1186/s40623-018-0867-8

Miyoshi, Y., Shinohara, I., Takashima, T., Asamura, K., Higashio, N., Mitani, T., et al. (2018). Geospace exploration project ERG. *Earth, Planets and Space*, *70*(1), 101. https://doi.org/10.1186/s40623-018-0862-0

Nishimura, Y., Gallardo-Lacourt, B., Zou, Y., Mishin, E. V., & Knudsen, D. J. (2019). Magnetospheric signatures of STEVE: Implication for the magnetospheric energy source and inter-hemispheric conjugacy. *Geophysical Research Letters*, *46*, 5637–5644. https://doi.org/10.1029/2019GL082460

Ogawa, Y., Tanaka, Y., Kadokura, A., Hosokawa, K., Ebihara, Y., Motoba, T., et al. (2020). Development of low-cost multi-wavelength imager system for studies of aurora and airglow. *Polar Science*, *23*, 100501. https://doi.org/10.1016/j.polar.2019.100501

Okano, S., & Kim, J. S. (1987). Observations of a SAR-arc associated with an isolated magnetic substorm. *Planetary and Space Science*, *35*(4), 475–482. https://doi.org/10.1016/0032-0633(87)90104-8

Partamies, N., Amm, O., Kauristie, K., Pulkkinen, T. I., & Tanskanen, E. (2003). A pseudo-breakup observation: Localized current wedge across the postmidnight auroral oval. *Journal of Geophysical Research*, *108*(A1), 1020. https://doi.org/10.1029/2002JA009276

Prölss, G. W. (2006). Subauroral electron temperature enhancement in the nighttime ionosphere. *Annales de Geophysique*, *24*(7), 1871–1885. https://doi.org/10.5194/angeo-24-1871-2006

Pryse, S. E., Kersley, L., Williams, M. J., & Walker, I. K. (1998). The spatial structure of the dayside ionospheric trough. *Annales de Geophysique*, *16*(10), 1169–1179. https://doi.org/10.1007/s00585-998-1169-4

Rees, M. H., & Roble, R. G. (1975). Observations and theory of the formation of stable auroral red arcs. *Reviews of Geophysics*, *13*(1), 201–242. https://doi.org/10.1029/RG013i001p00201

Rodger, A. S., Moffet, R. J., & Quegan, S. (1992). The role of ion drift in the formation of ionization troughs in the mid- and high-latitude ionosphere—A review. *Journal of Atmospheric and Terrestrial Physics*, *54*(1), 1–30. https://doi.org/10.1016/0021-9169(92)90082-V

Sakaguchi, K., Shiokawa, K., Miyoshi, Y., Otsuka, Y., Ogawa, T., Asamura, K., & Connors, M. (2008). Simultaneous appearance of isolated auroral arcs and Pc 1 geomagnetic pulsations at subauroral latitudes. *Journal of Geophysical Research*, *113*, A05201. https://doi.org/10.1029/2007JA012888

Sangalli, L., Partamies, N., Syrjäsuo, M., Enell, C.-F., Kauristie, K., & Mäkinen, S. (2011). Performance study of the new emCCD-based all-sky cameras for auroral imaging. *International Journal of Remote Sensing*, *32*(11), 2987–3003. https://doi.org/10.1080/01431161.2010.541505

Shiokawa, K., Katoh, Y., Hamaguchi, Y., Yamamoto, Y., Adachi, T., Ozaki, M., et al. (2017). Ground-based instruments of the PWING project to investigate dynamics of the inner magnetosphere at subauroral latitudes as a part of the ERG-ground coordinated observation network. *Earth, Planets and Space*, *69*(1), 160. https://doi.org/10.1186/s40623-017-0745-9

Shiokawa, K., Miyoshi, Y., Brandt, P. C., Evans, D. S., Frey, H. U., Goldstein, J., & Yumoto, K. (2013). Ground and satellite observations of low-latitude red auroras at the initial phase of magnetic storms. *Journal of Geophysical Research: Space Physics*, *118*, 256–270. https://doi.org/10.1029/2012JA018001

Siefring, C. L., Amatucci, W. E., & Rodriguez, P. (1998). Fast electron temperature measurements with Langmuir probes: Considerations for space flight and initial laboratory tests. In R. F. Pfaff, E. Joseph, D. Borovsky, T. Young (Eds.), *Measurement techniques in space plasmas: Particles*, *Geophysical Monograph Series* (pp. 55–60). Washington, DC: American Geophysical Union. https://doi.org/10.1029/GM102p0055

Slater, D.W., & Kleckner, E.W. (1989). Stable auroral red arc occurrences detected by the Pacific Northwest Laboratory photometer network: A decade of observations, 1978–1988. United States: N. p. Web. https://doi.org/10.2172/5354921

Søraas, F., Laundal, K. M., & Usanova, M. (2013). Coincident particle and optical observations of nightside subauroral proton precipitation. *Journal of Geophysical Research: Space Physics*, *118*, 1112–1122. https://doi.org/10.1002/jgra.50172

Spasojević, M., Frey, H. U., Thomsen, M. F., Fuselier, S. A., Gary, S. P., Sandel, B. R., & Inan, U. S. (2004). The link between a detached subauroral proton arc and a plasmaspheric plume. *Geophysical Research Letters*, *31*, L04803. https://doi.org/10.1029/2003GL018389

Takagi, Y., Shiokawa, K., Otsuka, Y., Connors, M., & Schofield, I. (2018). Statistical analysis of SAR arc detachment from the main oval based on 11-year, all-sky imaging observation at Athabasca, Canada. *Geophysical Research Letters*, *45*, 11,539–11,546. https://doi.org/10.1029/2018GL079615

Voiculescu, M., Nygrén, T., Aikio, A., & Kuula, R. (2010). An olden but golden EISCAT observation of a quiet-time ionospheric trough. *Journal of Geophysical Research*, *115*, A10315. https://doi.org/10.1029/2010JA015557

Voiculescu, M., Nygrén, T., Aikio, A. T., Vanhamäki, H., & Pierrard, V. (2016). Postmidnight ionospheric troughs in summer at high latitudes. *Journal of Geophysical Research: Space Physics*, *121*, 12,171–12,185. https://doi.org/10.1002/2016JA023360

Watkins, B. J. (1978). A numerical computer investigation of the polar F-region ionosphere. *Planetary and Space Science*, *26*(6), 559–569. https://doi.org/10.1016/0032-0633(78)90048-X

Zhang, Y., Paxton, L. J., Morrison, D., Wolven, B., Kil, H., & Wing, S. (2005). Nightside detached auroras due to precipitating protons/ions during intense magnetic storms. *Journal of Geophysical Research*, *110*, A02206. https://doi.org/10.1029/2004JA010498